UC Irvine
UC Irvine Electronic Theses and Dissertations

Title
Electrochemical Sensor for Salivary Detection of Malaria

Permalink
https://escholarship.org/uc/item/84r816jw

Author
Han, Jinny

Publication Date
2018

Peer reviewed|Thesis/dissertation

UNIVERSITY OF CALIFORNIA,

IRVINE

Electrochemical Sensor for Salivary Detection of Malaria

THESIS

submitted in partial satisfaction of the requirements

for the degree of

MASTER OF SCIENCE

in Biomedical Engineering

by

Jinny Han

Thesis Committee:

Professor William C. Tang, Chair

Professor Michelle Khine

Professor Michelle A. Digman

2018

DEDICATION

To

my mother

Mrs. Michelle Han

for your love and support

TABLE OF CONTENTS

Page

LIST OF FIGURES

LIST OF TABLES

ACKNOWLEDGMENTS

I would like to show deepest gratitude to my committee chair and mentor, Professor William C. Tang, for the opportunity to work on this project and for all the patience and effort he graciously provided to guide me through engineering concepts and research. Without his guidance, this thesis would not have been possible.

I would like to show appreciation for my committee members, Professor Michelle Khine and Professor Michelle A. Digman, for their kindness in giving me their valuable time.

A big thank you to Khine lab for generously providing materials and equipment for fabrication.

Finally, I would like to thank my family and friends for all their encouragement and support.

ABSTRACT OF THE THESIS

Electrochemical Sensor for Salivary Detection of Malaria

By

Jinny Han

Master of Science in Biomedical Engineering

University of California, Irvine, 2018

Professor William C. Tang, Chair

Global surveillance by the World Health Organization (WHO) has indicated a large stagnancy over the past few years in global efforts to eliminate malaria. Limited access to health care and proper diagnosis for endemic populations were emphasized as factors that attribute to such high morbidity and mortality rates. Rapid diagnostics tests (RDTs) have been reported to mitigate these factors, as well as other contributors to disease prevalence. The purpose of this thesis is to further demonstrate the feasibility of developing a quantitative, label-free RDT for disease biomarkers. The scope of this study is limited to the detection of plasmodium lactate dehydrogenase (pLDH) by electrochemical impedance spectroscopy (EIS) analysis of aptamer-protein complex formation as self-assembling monolayers (SAMs) on gold interdigitated electrodes (IDE). Notably, a Wheatstone bridge is integrated into the sensor design, improving system stability for accurate detection of pLDH in low concentrations. This demonstrates the feasibility of salivary detection of *Plasmodium falciparum* as a noninvasive method of malaria detection, which is especially important for addressing the needs of children in developing countries, who encompass a large portion of the global endemic population. To demonstrate [portability and cost-effectiveness, simple hardware was implemented in the design of this device. Together, the

biosensor and hardware are designed to innovatively detect the charge transfer resistance (R_{ct}) of an electrified interface as a simple impedance difference without the high costs and complexities of modern EIS instrumentation. The frequency domain of three different sensor designs will be analyzed for sensor optimization.

1.1 Introduction to malaria

Malaria is caused by the *Plasmodium* parasite. When a female *Anopheles* mosquito feeds on an infected human, parasites traverse its midgut, and enter the salivary glands, where they mature into sporozoites. During a blood meal, the mosquito injects its saliva to transport the parasite, along with biomolecules that mitigate barriers to feeding by the host immune response. The constituents of transmitted saliva are essential for further development of sporozoites within the human host [1]. Within 45 minutes, sporozoites clear the bloodstream and begin reproduction within hepatocytes. Currently, five species of *Plasmodium* are known to cause malaria in human hosts. Among these, *P. falciparum*, and recently *P. vivax* are the main culprits of malaria-induced fatalities [2].

1.2 Significance and motivation

Global surveillance has indicated an increase in malaria case incidences by five million from 2015 to 2016. Among 91 countries affected, 216 million cases and 445,000 deaths were reported. While morbidity and mortality rates have significantly declined since 2010, the rate of decline has been decreased or reversed since 2014. The WHO Africa region continues to attribute to 90% of the reported cases, with children under 5 years old at the highest risk for fatalities [3].

1.3 Current methods of malaria detection

1.2.2 Giemsa Microscopy

Giemsa microscopy has remained the gold standard for laboratory diagnosis of malaria for over a century due to its simplicity and low cost. Blood samples are prepared on a glass slide for examination under a light microscope. A thick film is examined to quantify parasites while a thin film enables morphological differentiation among species. Giemsa microscopy provides species discrimination and assessment of parasite density. However, endemic regions the lack experts and trained workers required to meet such time consuming and intensive labor demands. Moreover, this method is relatively low in sensitivity. While experts can detect as low as 5 parasites/µL, the average technician has a detection limit of 50-100 parasites/µL [4]. In most endemic regions, this technique is not suitable for routine diagnosis.

1.2.4 Polymerase Chain Reaction

Developments in molecular techniques are continually providing new strategies for diagnosis. Polymerase chain reaction (PCR) has been widely implemented for parasite nucleic acid detection with higher sensitivity and specificity than light microscopy [5]. However, the time required to obtain results limits PCR implementation in healthcare settings. Implementation in endemic regions is also limited due to the high costs of equipment and training [6].

1.2.5 Rapid Diagnostic Tests

Rapid diagnostic tests (RDT) provide cost efficiency and ease of use in malaria detection. The use of RDTs in malaria detection has significantly grown since the WHO recognized the need for alternative methods to supplement conventional microscopy [7]. RDTs have been accepted by endemic regions as reliable and greatly beneficial in malaria diagnosis, especially in rural areas lacking healthcare facilities [8].

1.3 Malaria detection in saliva

Current detection methods require blood sampling for accurate diagnosis. This approach can be uncomfortable for young children and introduces the potential for disease transmission. Alternatively, saliva is a promising diagnostic fluid for safe and convenient detection.

Saliva has been demonstrated to be an effective sample for malaria detection through sensitivity and specificity assessments based on microscopically confirmed cases. Ghobotosho *et al.* reported a 100% specificity and 77.9% sensitivity for *Pf*LDH detection in whole saliva of 130 children in Nigeria with *P. falciparum* infection [9]. Fung *et al.* demonstrated the quantitative detection of *Pf*HRP2 in saliva samples from patients with microscopically confirmed *P. falciparum*. Custom chemiluminescent ELISA on samples stabilized with protease inhibitors revealed salivary levels ranging from 17 to 1,167 pg/mL [10].

1.5 Chapter Summary

Malaria remains a serious issue with significant impact on endemic regions. Rapid detection followed by appropriate treatment is the key towards the goal of eliminating malaria. RDTs provide the simplicity and reliability suited for endemic regions lacking resources and improves malaria detection to

compensate for the limitations of conventional methods with affordability. Recently, saliva has gained

attention as a candidate sample fluid for noninvasive malaria detection. Saliva sampling provides

convenience for routine monitoring without the risk of infected disease transmission introduced by

blood sampling. RDTs for salivary detection of malaria have great potential in reducing misdiagnosis and

improving disease monitoring and patient care.

CHAPTER 2: DETECTION APPROACH

2.1 Electrochemical Impedance Spectroscopy

Electrochemical Impedance Spectroscopy (EIS) is a powerful method for investigating material properties by exploiting the frequency dependence of electrochemical systems. Impedimetric measurements are analyzed to characterize and investigate materials of interest [11]. EIS has been significantly applied to the development and evaluation of sensors.

2.1.1 Introduction to EIS

An electrochemical cell is composed of electrolyte, electrodes, and the material to be characterized. A combination of up to three electrodes are configured to serve unique purposes for measurement and analysis. These electrodes are referred to the Working Electrode (WE), the Reference Electrode (RE), and the Counter Electrode (CE) as shown in figure 2.1a. In practice, the excitation signal is applied to the WE to form an electrified interface on which a redox reaction occurs (fig 2.1b). The CE prevents interference of the reaction at the WE by the production of electroactive species. The CE is typically a large inert metal configured to form a closed circuit [12]. A RE may be integrated to provide a reference for measurements at the WE.
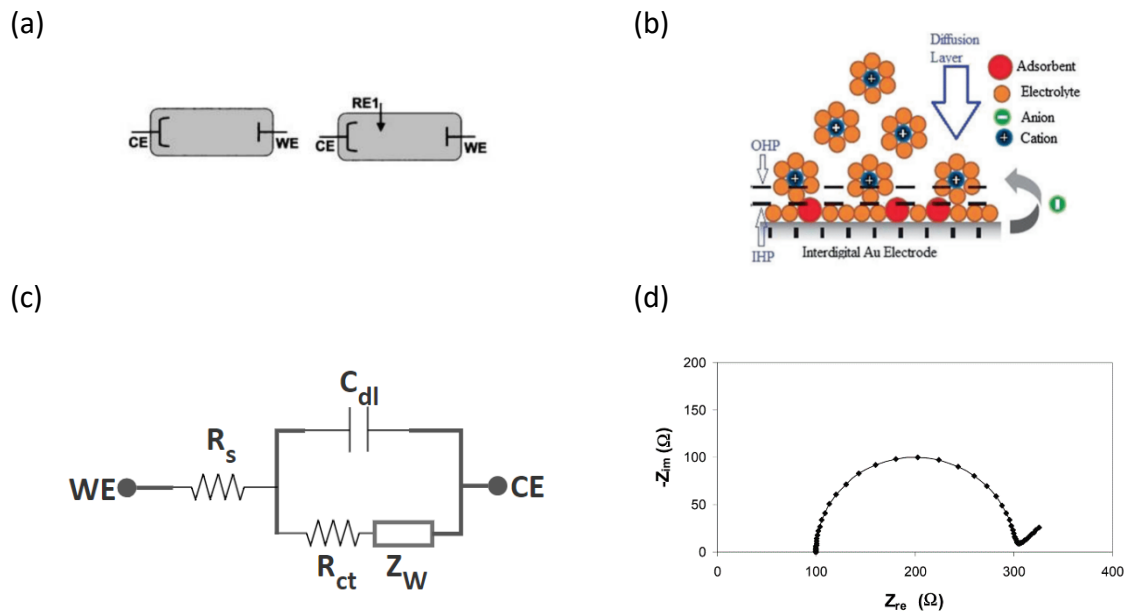
(a)

(b)

(c)

(d)

Figure 2.1: (a) Three electrode types configured as two electrochemical cell types [13]. (b) The electrified interface. (c) A Randles cell with kinetic control and its (d) resulting Nyquist plot.

Physical factors that affect the impedance of the system are typically modeled as equivalent electric circuit (EEC) elements for mathematical estimation of unknown properties. The most commonly used circuit model is the Randles cell. The Randles cell was developed as a tool for calculating reaction kinetics of rapid systems without the complexities of fluid dynamics. A Randles cell with kinetic control, shown in figure 2.1c, consists of three EEC elements: solution resistance (R_S), double layer capacitance (C_{dl}), charge transfer resistance (R_{CT}). R_s is the resistance of the solution bounded system. C_{dl} accounts for the separation of charges between the electrode and ions caused by the absorption of ions onto the electrode surface. The formation of this double layer exhibits capacitive behavior. R_{CT} arises in kinetically controlled reactions and represents the resistance to charge transfer at the electrified interface. The diffusion of species involved in oxidation and reduction determines electron transfer rate and thus reaction speed [12]. In systems involving kinetic control, diffusion displays impedance characteristics known and modeled as Warburg impedance (Z_W). Z_W is low in response to high excitation frequencies,

while high in response to low excitation frequencies. This can be explained by the inverse relationship between the excitation frequency and the diffusion distance [13]. Measurements are typically displayed in a Nyquist plot, as shown in figure 2.1d.

2.1.2 Biosensor applications of EIS

EIS has been implemented in biosensors for direct transduction of altered electrochemical properties into electrical signals. Impedimetric biosensors recognize the formation of a molecular complex between a target biomolecule and a modified electrode surface. This technique has been demonstrated to recognize many biological targets such as nucleic acids, proteins, microorganisms, cells, antibodies and antigens. Fitting data obtained from impedance measurements with a verified EEC model enables calculation of impedance parameters of interest, and a direct relation between the detected analyte concentration and overall impedance can be made [14].

Surface treatment of electrodes with self-assembling monolayers (SAMs) enables the capture of specific biomolecules. The monolayer of impedimetric biosensors are often constructed with long-chain thiols to form stable bonds with gold electrodes. Various methods can be utilized to generate a functional monolayer with high affinity to a target molecule. Deposition of a Langmuir-Blodgett film onto the electrode surface is a commonly employed technique. Exposure to a liquid solution containing functionalized SAMs results in spontaneous chemisorption and self-organization of molecules into a film [15].

The measurement of a recognition event is not limited to impedance changes. The presence of target molecules can be determined as a change in capacitance. Immobilized biomolecules induce a change in dielectric constant or thickness of the surface double layer, causing capacitance changes in the capacitive double layer [16]. Sensitive detection of interferon-γ with SAMs modified for antibody

immobilization has been demonstrated to achieve sensitive capacitance measurements. Alternatively, resistive sensors measure the change in the rate of charge transfer induced by a bound analyte. Glycoprotein associated with human mammary tumors was successfully detected as a change in charge transfer resistance. This method often involves the presence of a redox couple such as the ferri-/ferrocyanide system. Highly sensitive detection is achieved when the applied potential is equal to the open circuit potential of the redox couple [14].

2.2 Detection of pLDH with aptamers

The emergence of aptamers as a promising class of recognition molecules significantly extend the possibilities of impedimetric transduction. Aptamers are oligonucleotides that are synthesized to specifically bind to a target with high affinity and specificity. Unlike antibodies, aptamers are not limited by low immunogenicity or toxicity, and are capable of economic mass production [17]. Furthermore, the aptamer selection process can be modified to obtain other desired attributes, such as thermal stability, for unlimited applications [18].

Several aptamers against pLDH have been described in literature. Cheung *et al.* found the 2008s aptamer by counterselection of closely related human lactose dehydrogenase (LDH) homologs. The 2008s aptamer was shown to bind a substrate specificity loop unique to P*f*LDH with a dissociation constant of 42 nM [19]. The pL1 aptamer found by Lee *et al*. was reported to bind both P*v*LDH and P*f*LDH with greater affinity at 16.8 ± 0.6 nM and 38.7 ± 1.3 nM, respectively (fig 2.2a-b)

Figure 2.2 c-d shows plots resulting from electrochemical detection of P*v*LDH. The change in charge transfer resistance on a Nyquist plot revealed a linear relationship between pLDH concentration and Rct on a log scale. Clinical implementation revealed a detection limit of 1 parasite/µL corresponding to an Rct value of 6 kΩ [19]. This demonstrates quantitative detection of malaria [20].
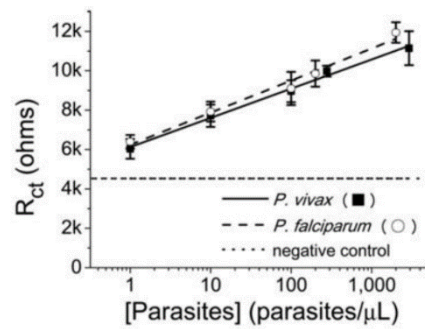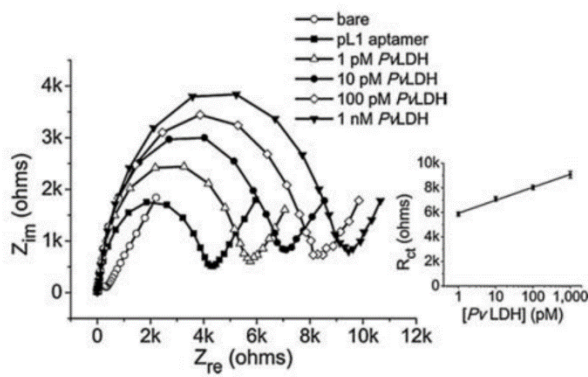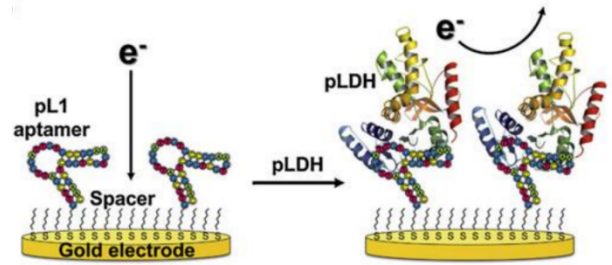
(a)
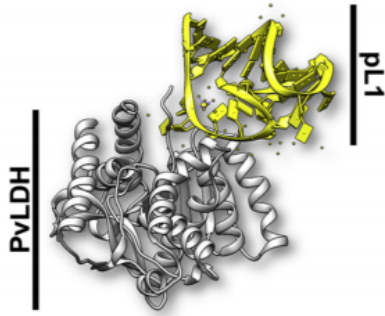
(b)

Figure 2.2: (a) pL1-pLDH tertiary binding complex [21]. (b) Schematic of electrochemical pLDH detection. (c) Nyquist plot of R_{ct} measurements across varying PvLDH concentrations. (d) Relationship between R_{ct} and parasite concentration

2.3 Wheatstone bridge

EIS instrumentation has evolved to obtain impedance information with extraordinary sensitivity and high efficiency, such that physical behaviors causing perturbation from steady state can be considered of little importance [22]. AC bridging enables accurate EIS data collection by mitigating these deviations without the high costs of EIS equipment [11].

The Wheatstone bridge is often utilized to measure an unknown resistance. Initially, identical resistors are separately set in parallel from each other, while in series with an adjustable resistor and

the device under test (fig #). R_2 is adjusted until the difference between the outputs are zero. Since R_1, R_2 and R_3 are known, R_x can be calculated as $R_1/R_2 = R_3/R_x$.
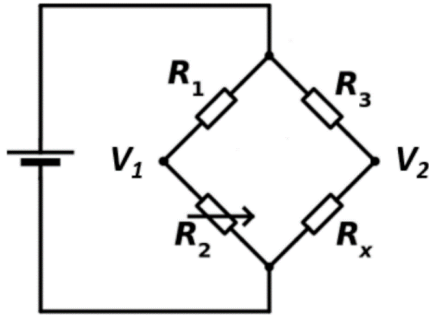
(a)   (b)
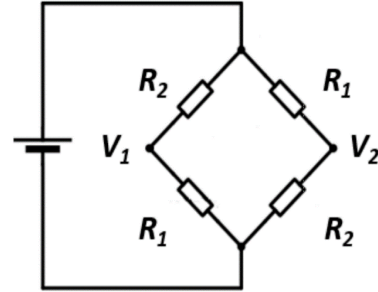

Figure 2.3: Wheatstone bridge configuration for measuring (a) unknown resistance and (b) differential voltage.

For sensing applications, voltage is applied across the Wheatstone bridge, and the differential voltage is used to measure a change in resistance. Initially, the four elements are identical and have known resistance values (R_1). Small changes applied to two opposing elements change the resistance values (R_2) to the configuration in figure (#). The change in resistance (ΔR) can be calculated through differential measurement of output voltages as shown in equation (1). This technique can be applied to a capacitive sensor to measure a change in impedance [23].

$$V_{out} = V_2 - V_1 = \frac{\Delta R}{2R_0 + \Delta R} V_S \qquad (1)$$

2.4 Chapter Summary

EIS is a powerful technique for analyzing material properties and has been extensively implemented in impedimetric biosensors coated with SAMs. Sensitive detection can be achieved by measuring a change in reaction speed in the presence of a target biomarker. Aptamers have unlimited potential for specific targeting and have been demonstrated to successfully detect pLDH. Through modifications of the aptamer selection process, it is possible to detect pLDH unique to parasite species. The pL1 aptamer is notable for its high binding affinity and was demonstrated to detect malaria at low concentrations through EIS. However, the complexities and high expense required for EIS render it unsuitable for routine diagnosis. The device described in the next chapter circumvents the complexities and high expense of EIS analysis. Through implementation of the Wheatstone bridge, impedance measurements can be simplified to a differential voltage measurement.

CHAPTER 3: DEVICE DESIGN

3.1 Design overview

The high cost of equipment and training required for EIS limits its potential for use in routine diagnosis of malaria. The device described in this chapter aims to overcome these limitations. EIS implementation on a Wheatstone bridge effectively simplifies impedance measurements to a differential voltage.
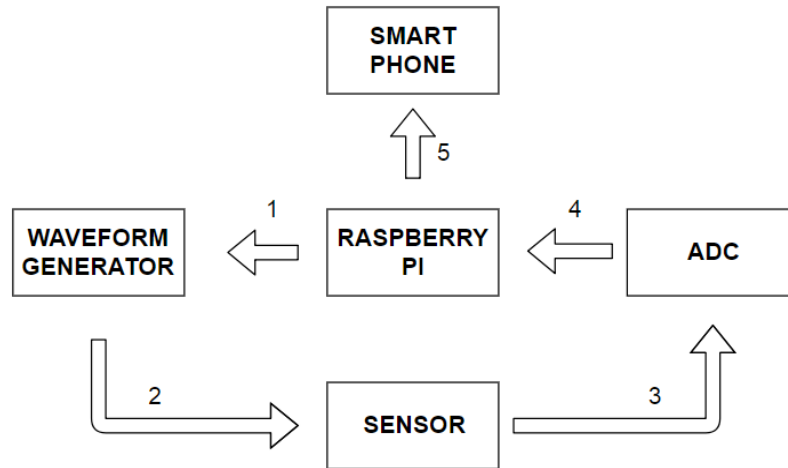
Figure 3.1: Diagram of hardware implementation

A diagram of the hardware to be implemented is shown in figure 3.1. The device consists of a gold electrode and simple hardware using the Raspberry Pi, a waveform generator, and an analog-to-digital converter (ADC). The Raspberry pi can be programmed to generate a small excitation at a specified frequency signal across the sensor through the waveform generator. The differential output voltage can then be read by the ADC, which digitizes the signal to be read by the Raspberry pi. The

digitized signal can be converted to a corresponding parasite concentration for display on a smartphone through further programming.

3.2 Capacitance simulations

Capacitance of gold sensors embedded on printable circuit board (PCB) was simulated on COMSOL to optimize the sensitivity to impedance changes while maintaining tolerance to manufacturer variability. Simulations of the bare components of the Wheatstone bridge were performed with varying electrode finger width and spacing between fingers within a constant area. Figure 3.2 compares variability in capacitance in response to changes in finger width by 10 μm increments and indicates a decrease in tolerance when spacing is increased. Furthermore, trends with identical spacing are very similar in comparison to trends with identical finger widths. This indicates that spacing may have a greater effect on capacitance than the finger width.
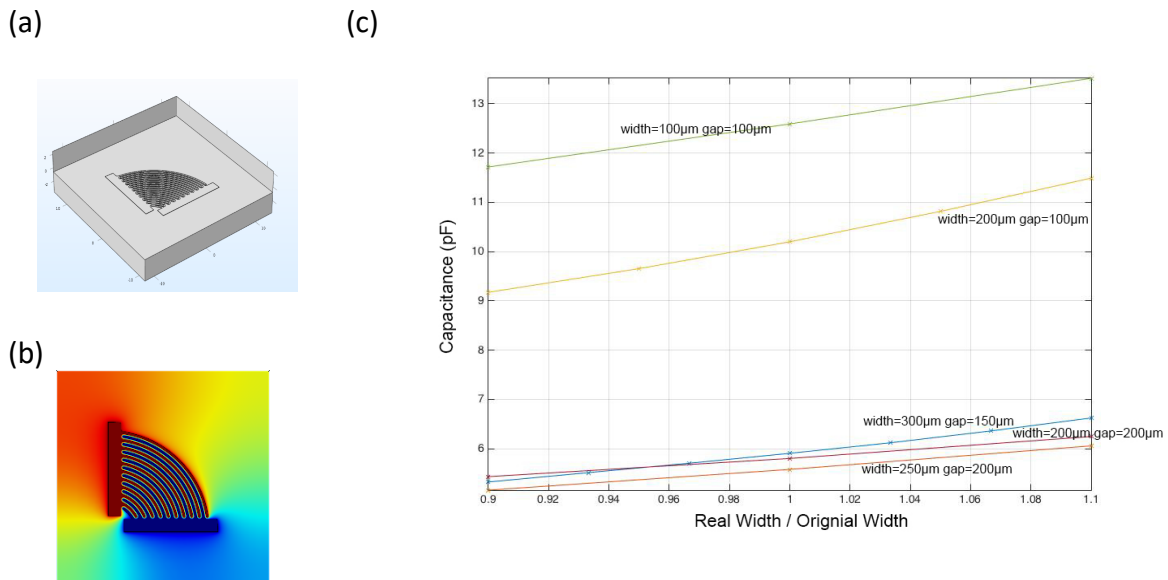
(a)   (c)

(b)

Figure 3.2: (a) Capacitance simulation on PCB. (b) Electric field distribution. (c) Graph of capacitance simulations for manufacturing errors

Three electrode designs were fabricated with the following geometric parameters: 160 μm fingers spaced 160 μm apart designated 1616, 200 μm fingers spaced 200 μm apart designated 2020, 250 μm fingers spaced 200 μm apart designated 2520. Simulated capacitance values are listed in table 1.

Electrode	1616	2020	2520
Capacitance	7.15 pF	6.00 pF	5.36 pF

Table 3.1: Simulated capacitance values of each electrode

3.3 Sensor specifications

The general design features four interdigitated electrodes (IDEs) configured to form a Wheatstone bridge as shown in figure 3.3a-b. Each node is merged to form a circle with a diameter of 24 mm to minimize the overall area.

(a)
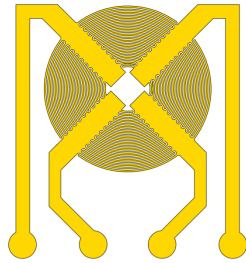
(b)

(c)

Figure 3.3: (a) Illustration of sensor design. (b) Microscopic image. (c) EEC model of one section

3.2.2 EEC model

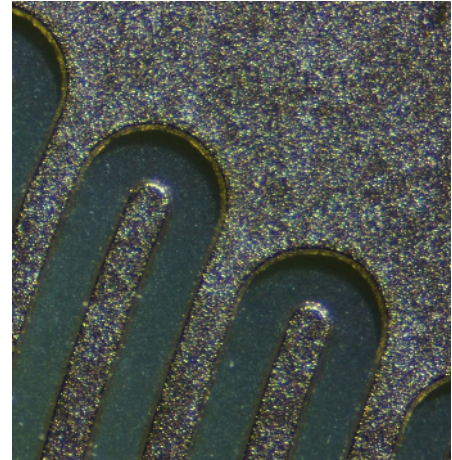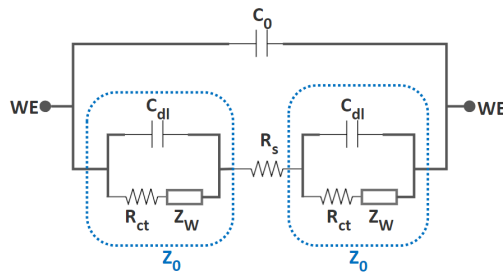EEC models are known to be most useful when the model accurately represents the system while maintaining simplicity. However, the simplified Randles cell often falls short due to the complexity of system dynamics and its dependence on numerous environmental and system-specific factors. The model is suitable as a foundation to build upon [12].

The EEC model is shown in figure 3.3c. The four sections of the interdigitated electrodes can be represented as a two electrode setup, which combines the function of the reference electrode into a counter electrode and a working electrode. The counter electrode is accounted for when a closed circuit is formed to test the electrode. Therefore, both electrodes can be set as WE for improved sensitivity to impedance changes. To account for this difference, the solution resistance R_s is positioned in between two working electrodes in series. Each interface at the working electrode is represented with elements of a Randles cell with kinetic control. Fouble-layer capacitance (C_d) is positioned in parallel to the charge transfer resistance (R_{ct}) in series with Warburg impedance (Z_W). The overall capacitance C_0 is in parallel with the entire two-electrode configuration.

3.2.2 Calculating impedance

Impedance at each interface can be calculated from the EEC model as shown in equation (2) where it is represented as Z_0. The total impedance of two interdigitated sections is represented as Z_1 in equation (3), which is further expanded to equation (4) by substituting Z_0.

$$Z_0 = \frac{R_{ct} + Z_W}{1 + j\omega\, C_d\,(R_{ct} + Z_W)} \tag{2}$$

$$Z_1 = \frac{R_s + 2Z_0}{1 + j\omega\, C_0\,(R_s + 2Z_0)} \tag{3}$$

$$= \frac{R_s + 2\,(R_{ct} + Z_w) + j\omega\, R_s C_d\,(R_{ct} + Z_W)}{1 + j\omega[(C_d + 2C_0)(R_{ct} + Z_W) + C_0 R_s] - \omega^2\, C_0 C_d\, R_s(R_{ct} + Z_W)} \tag{4}$$

Z_1 represents two opposing sections of the Wheatstone bridge coated with pL1 as a recognition layer for pLDH. To form a Wheatstone bridge for differential measurement, the remaining two opposing sections are investigated as bare sections in the same solution. The bare sections of the Wheatstone sections can be modeled by positioning the overall capacitance C_0 in parallel with solution resistance R_s. The impedance of bare electrodes is represented as Z_2 as shown in equation (5). Substituting impedance into equation (2) from chapter 2.3 results in equation (6), which relates impedance to differential voltage.

$$Z_2 = \frac{R_s}{1 + j\omega C_0 R_s} \tag{5}$$

$$V_{out} = V_{in}\frac{Z_1 - Z_2}{Z_1 + Z_2} \tag{6}$$

16

$$= V_{in} \frac{Z_0}{R_s + Z_0 + j\omega\, C_0\, R_s (R_s + 2Z_0)}$$

$$(7)$$

$$= V_{in} \frac{1}{1 + 2j\omega\, C_0\, R_s + R_s(j\omega\, C_0\, R_s + 1)\dfrac{1 + j\omega\, C_d\, (R_{ct} + Z_W)}{R_{ct} + Z_W}} \qquad (8)$$

Equation (8) shows that V_{out} can be maximized with a small C_0. However, simulated C_0 values described in the previous section were very low, meaning its effect on V_{out} is relatively low. Furthermore, the effect of ω on Z_W complicates the relationship between V_{out} and ω. While equation (8) conveys an inverse relationship between V_{out} and ω, the signal cannot be optimized by minimizing ω. Doing so increases the limitations of the equation due to the introduction of more complexities in system dynamics accumulated over time. The effect of Z_W requires experimental analysis the frequency domain.

3.4 Chapter summary

The device was designed to innovatively reduce the complexities of EIS by detecting impedance changes as a differential voltage measurement from a Wheatstone bridge in a cost-efficient manner. Through capacitance simulations, interdigitated electrodes with three different geometries were designed. The width of electrode fingers and the gap distance separating them were chosen to optimize sensitivity and tolerance to manufacturing error. An EEC model provided some insight on the effects of impedance parameters on differential voltage. Simplicity and cost efficiency can be achieved through basic hardware implementation.

CHAPTER 4: FABRICATION AND METHODS

4.1 SENSOR FABRICATION ON PCB

Printable circuit boards (PCB) are an essential component of electronic circuits manufactured in nearly all computational electronics such as cell phones and calculators. Its purpose is to provide mechanical support and electronic connections to route signals.

4.1.1 PCB fabrication

PCB is most often fabricated by photoengraving copper foil on fiberglass. A photoresist is first applied to the substrate, making it photosensitive. Patterning copper foil requires the design of a mask to specify areas to be etched away. The mask is placed above the substrate so that only unmasked areas are affected by exposure to UV light. When a negative photoresist is used, exposure hardens the photosensitive substrate so that softer masked regions are etched away when exposed to a solvent. Alternatively, a positive photoresist softens upon exposure so that unmasked regions are dissolved [24].

The three electrode designs were drawn on AutoCAD and filled with copper tracing on EAGLE. A solder mask, board layout, and copper tracing were sent to be manufactured. The electrodes were fabricated on two-layer boards (38.02x45.54mm).

4.1.2 Gold surface finish

The fabricated electrodes feature an Electroless Nickel Immersion Gold (ENIG) finish. A PCB surface finish promotes reliable connectivity to other circuit components. Moreover, gold is

biocompatible and highly resistant to corrosion [25]. An ENIG finish is well-suited for the sensor as it provides a flat, uniform surface [26].

The ENIG process involves a series of reactions among metals and solution. Exposing copper and another metal, such as palladium, to an activating solution results in simultaneous anodic and cathodic reactions at the copper surface. The displacement reaction results in copper fully plated with palladium, which acts as the catalytic surface during electroless nickel plating. In the presence of a catalyst, a source of nickel and a reducing agent undergo a redox reaction. The reduction of nickel results in the deposition of a nickel layer. A second displacement reaction is required to generate a gold layer above the nickel, finalizing the gold finish [27].

4.2 Solution chamber fabrication

To form a Wheatstone bridge, the two opposing sections to be functionalized must be exposed to the same condition. The aptamer solution must be maintained in a constant boundary throughout the 14-hour functionalization time. A chamber with four divisions separates the four sections of the electrode. Polydimethylsiloxane (PDMS) was initially chosen as the chamber material for its mechanical flexibility. PDMS is inert and biocompatible, making it well-suited for biotechnology applications. However, leak prevention overnight was not guaranteed. The mold assembled with 3D printed chamber components often resulted in slow leakage due to the small gap between the PDMS chamber and the PCB is formed by the copper traces. Water and saline solution were found to be ill-suited for trials due to the low surface tension of the aptamer solution. After repeated attempts, an alternative form of PDMS was implemented.

A PDMS-based adhesive polymer was used to create a reversible seal between the chamber and sensor. The adhesive polymer is composed of PDMS and a silicone-based soft skin adhesive. The weight

19

ratio of the two components determine the tackiness and stickiness of the resulting polymer [28]. For chamber fabrication, the components were mixed at a 1:1 ratio for 10 minutes, degassed, and poured into laser cut acrylic molds. Unlike PDMS, the adhesive polymer can be easily removed from acrylic without prior silane treatment. After baking at 60°C for 30 minutes, a layer of uncured PDMS, mixed (1:10) and degassed, was poured above the cured adhesive polymer layer to provide structure. A 1:2 weight ratio of adhesive polymer to PDMS resulted in a chamber with reliable adhesion and structural stability.
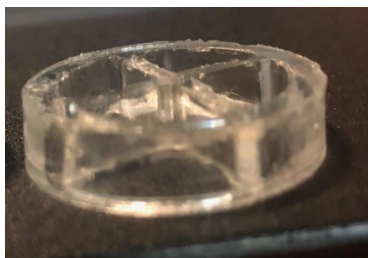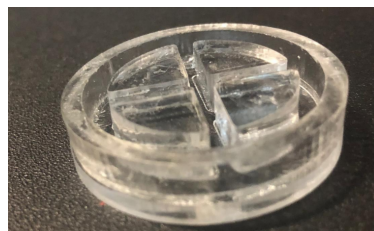
(a)   (b)

Figure 4.1: (a) Adhesive polymer chamber for functionalization. (b) Laser cut acrylic mold

4.2 Sensor preparation

4.2.1 Gold surface cleaning

To obtain accurate measurements from the sensor, the quality of the gold surface must be in optimal condition. Impurities resulting from exposure to the environment leads interferes with monolayer formation [29]. The electrode was subject to a combination of electrochemical cleaning techniques prior to functionalization. The electrodes were first submerged in acetone for 10 minutes. The electrode was immersed in a mixture of 25% v/v H_2O_2 and 50 mM KOH for another 10 minutes, then

rinsed with DI water [30]. Finally, the electrode was placed in a 50 mM KOH solution and a potential

sweep of -800 mV to 1300 applied across the sensor at a scan rate of 50 mV/s for voltammetric cleaning

[31].

4.2.2 Sensor functionalization

The pL1 aptamer was resuspended to 100 uM and kept frozen in 10 mM Tris, 0.1 mM EDTA, pH

8.0. Prior to functionalization, the aptamer must be thiol-modified at its 5' end to bind the gold surface.

Disulfide bonds at the 5' end of the aptamer were reduced to thiol groups by adding 40 μL of 2.5 mM

Tris[2-carboxyethyl]phosphine (TCEP) for five hours at room temperature. The thiol-modified aptamer

was subsequently mixed with 20 μL 6-mercapto-1-hexanol and 2 mL phosphate buffered saline (PBS) pH

7.4 to form the aptamer solution. The spacer molecules provide adequate room for binding the target

molecule [32]. The gold surface of two opposing sections of the Wheatstone bridge were functionalized

by exposure to the aptamer solution for 14 hours at room temperature, as shown in figure 4.2 [20].

Functionalized electrodes were rinsed with DI water before measurements were taken.
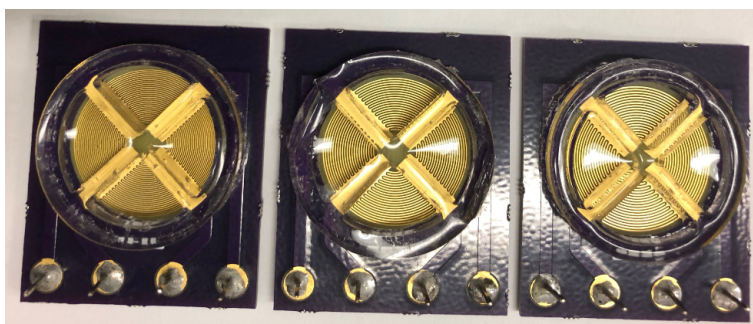

Figure 4.2: Functionalization of each electrode with adhesive polymer chamber.

21

4.3 Experimental Setup and Test

The basic hardware was incorporated in the design to replace a function generator and oscilloscope to develop a cost-efficient and portable device. Because the hardware could not be properly implemented, the setup in figure 4.3a-b was used for reliable waveform generation and voltage measurement.
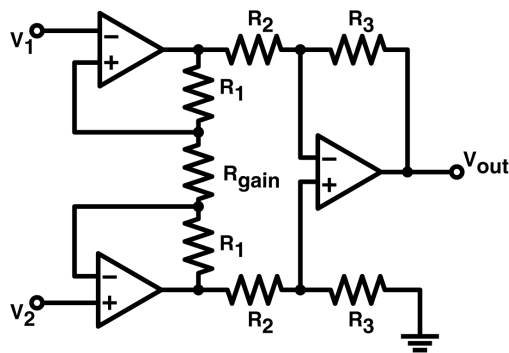
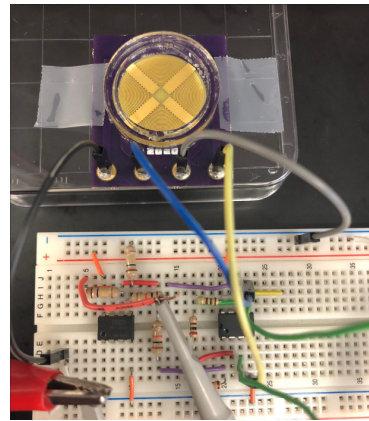(a)   (b)

Figure 4.3: (a) Instrumentation amplifier circuit. (b) Experimental setup for amplified voltage measurement

A testing chamber is required to maintain solution within a constant boundary and thus keep the system in steady state during testing. The adhesive polymer was well-suited for this application, as the functionalization chamber could be easily removed and replaced by the testing chamber.

The function generator (Agilent 3322A) was used to apply a 50 mV_{pp} sine wave across the electrode across maximum frequency range. The response was measured as a differential voltage with the oscilloscope (Agilent 54642D). Using the OPA1013D, an instrumentation amplifier setup was

implemented to improve the signal-to-noise ratio. The frequency vs gain characteristics of the chosen amplifier limited the maximum input frequency range to 70 kHz at a set gain of 20. The cutoff frequency was confirmed before any electrodes were tested.

4.4 Chapter summary

With modern PCB fabrication techniques, electrical circuits with microscale features can be easily mass-produced. The sensors were fabricated on PCB with an ENIG finish for a gold surface that is flat and uniform. Electrochemical cleaning was followed by functionalization of thiol-modified aptamers using chambers divided into four sections to form a Wheatstone bridge capable of differential measurement. Small output signals from the sensor were amplified with instrumental amplifier circuits for measurement with an oscilloscope. The circuit was shorted prior to each measurement taken in the presence of a redox couple to account for the accumulation of charges.

5.1 Electrodes coated with pL1

The frequency response of all three sensors are shown in figure 5.1. The RMS value of each measurement is shown. Results are not informative likely due to inconsistencies in experimental setup. The sensor was discharged prior to each measurement for each of the three board 2 electrodes and the second trial of the 2020 electrode. However, this was not implemented during the other trials. It is possible that the larger signals observed in these trials are a result of charge accumulation. Furthermore, signal attenuation displayed by electrode 2020 board 1 trial 2 and the large drop in observed in 1616 board 1 can likely be explained by damage from soldering and the amplifier gain.
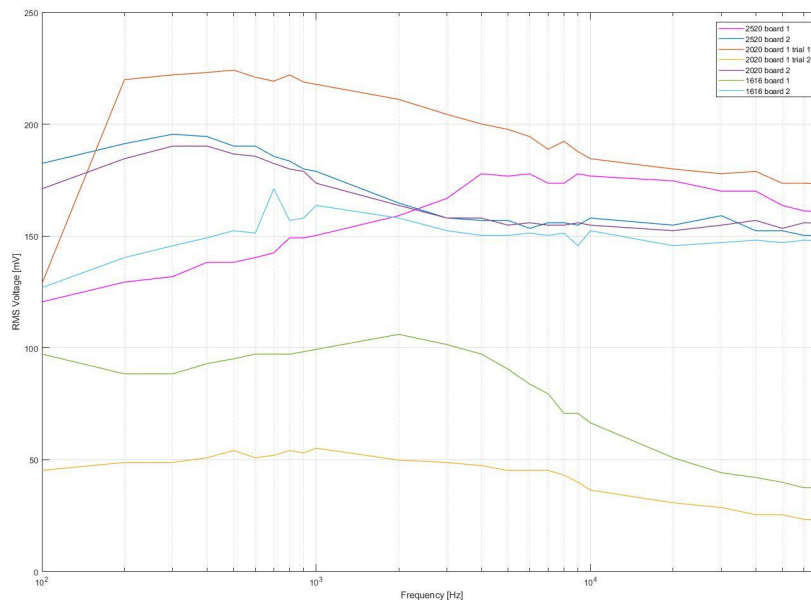

Figure 5.1: Results from trial runs of the electrodes coated with pL1

Figure 5.2 shows the frequency response characteristics of the three electrodes that were tested under the same conditions. The resulting graph indicates that sensitivity to impedance changes by pL1 coating is greatest in 2520 and least in 1616. Furthermore, the trends appear to be somewhat similar, especially between electrodes 2020 and 2520.
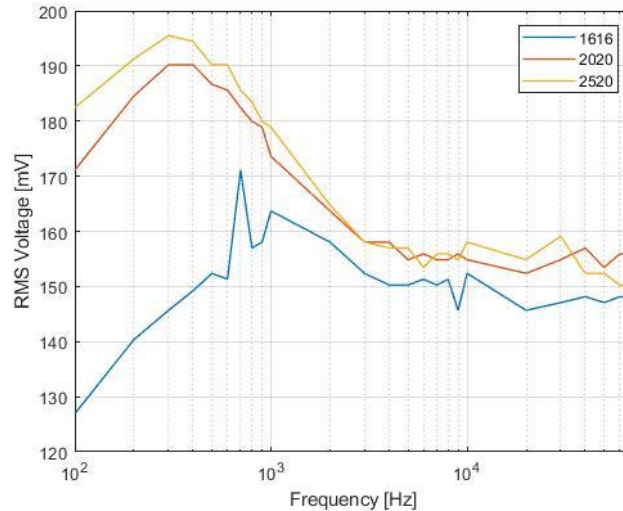

Figure 5.2: Results from trial runs of electrodes coated with pL1 under the same experimental conditions

5.1.1 Electrode 1616

Figure 5.3a illustrates the frequency response of two electrodes with finger widths of 160 μm separated by 160 μm when coated with the pL1 aptamer. The first board was tested with the initial amplifier gain of 100, while the second board was tested with a gain of 20. Consequently, the data resulting from the first board was limited by the amplifier, and signals were attenuated at around 30-40 kHz. However, the two boards show very different signals at frequencies before amplifier attenuation and no conclusions could be made.
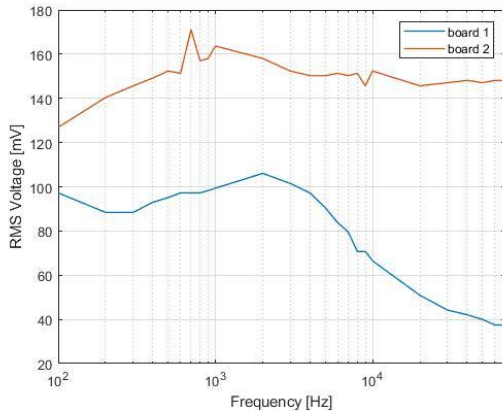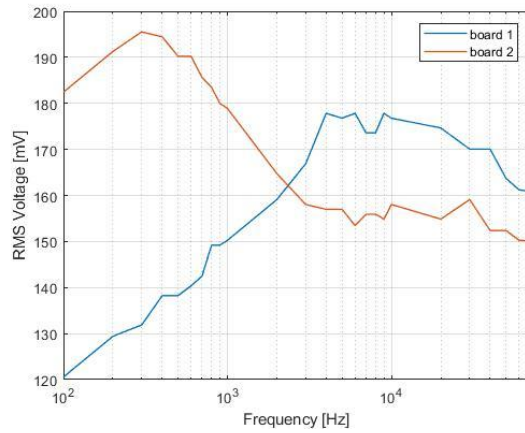
(a)   (b)

Figure 5.3: Comparison of results from two separate boards for both (a) the 1616 electrode and (b) the 2520 electrode

5.1.3 Electrode 2520

The electrodes with 250 µm finger widths separated by 200 µm resulted in very different

frequency response characteristics (fig 5.3b). Although trends begin to appear somewhat similar at

around 3-4 kHz, the lack of synchronization is observed at most frequencies. Trends appear

unsynchronized randomly, and no conclusions could be made.

5.1.2 Electrode 2020

The frequency response of the electrode with 200 µm wide fingers spaced 200 µm apart is

shown in figure 5.4a. Two separate trials were run for the first board while the second board was tested

once. Measurements from the 2020 electrode appear to have more consistency than the other two

electrodes. After the second trial of board 1, damage from re soldering was observed at the node

connected to the function generator. This may explain the attenuated signal across the entire frequency
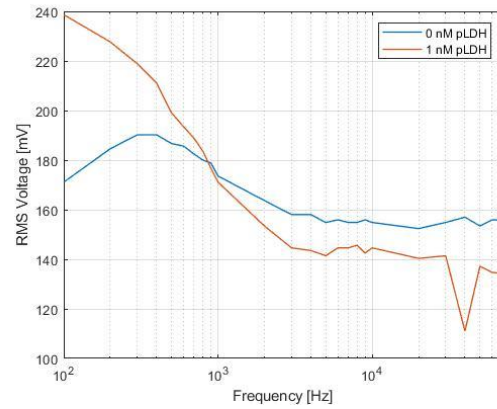
range.
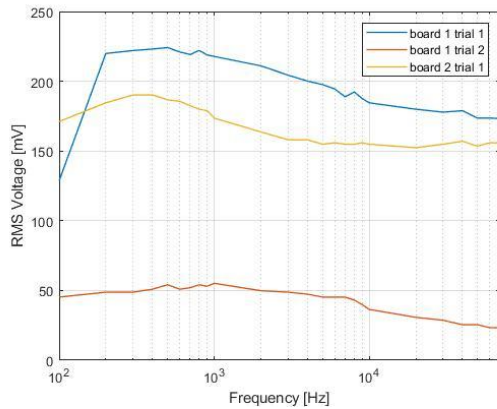
(a)   (b)

Figure 5.4: Comparison of results from the 2020 electrode (a) without pLDH and (b) with

pLDH

5.2 Electrode 2020 with pLDH

Data from positive controls were successfully gathered for electrode 2020 board 2 only (fig

5.4b). The negative control is represented by the data previously described. The positive control was

tested as a separate trial. An increase in impedance is observed at frequencies lower than 900 Hz. The

decrease in impedance observed at 1 kHz – 70 kHz is unexpected. However, no real conclusions could be

made due to the lack of trials, and inconsistencies observed in other electrodes.

5.3 Overall evaluation of work

The differential voltage measurements taken from electrodes coated with pL1 resulted in

somewhat similar trends. However, due the lack of data collected under the same experimental

conditions, no conclusions could be drawn about the actual frequency response characteristics of each

27

electrode. Overall, electrolyte chambers were fabricated to overcome the leaking issue during functionalization and testing, and the short circuiting procedure was implemented.

5.4 Future directions

To progress towards device completion, proper hardware must still be implemented. This requires an ADC converter capable of sampling and converting at a high rate. Furthermore, the ADC should feature signal amplification so that measurements are not limited by op amp characteristics. This would likely make possible differential measurement across a much larger frequency range.

5.5 Chapter summary

Although some similarities could be seen in the results, no conclusions could be made about the frequency response characteristics due to the lack of data. The hardware requires modification for proper implementation. Overall, signal drift observed during initial trial runs were resolved by implementing the short circuiting procedure and a reversible adhesive chamber.

REFERENCES

1. Drame, P., Poinsignon, A., Marie, A., Noukpo, H., Doucoure, S., Cornelie, S. and Remoue, F. (2013). New Salivary Biomarkers of Human Exposure to Malaria Vector Bites. Anopheles mosquitoes - New insights into malaria vectors.

2. Bartoloni, A. and Zammarchi, L. (2012). CLINICAL ASPECTS OF UNCOMPLICATED AND SEVERE MALARIA. Mediterranean Journal of Hematology and Infectious Diseases, 4(1), p.2012026.

3. World Health Organization (2017). World Malaria Report. Geneva: World Health Organization.

4. Payne, D. (1988). Use and limitations of light microscopy for diagnosing malaria at the primary health care level. Bulletin of the World Health Organization, 66(5), 621–626.

5. Morassin B., Fabre R., Berry A., Magnaval J. F. (2002). One year's experience with the polymerase chain reaction as a routine method for the diagnosis of imported malaria. Am J Trop Med Hyg, 66: 503-508.

6. Hanscheid T, Grobusch M. P. (2002). How useful is PCR in the diagnosis of malaria? Trends Parasitol, 18: 395-398.

7. Salako L. A., Akinyanju O., Afolabi B. M. (1999). Comparison of the standard Giemsa-stained thick blood smear with the Quantitative Buffy Coat Technique in malaria diagnosis in Nigeria. Niger Q J Hosp Med, 9: 256-269.

8. Erdman L. K., Kain K. C. (2008). Molecular diagnostic and surveillance tools for global malaria control. Travel Med Infect Dis., 6: 82-99.

9. Gbotosho, G. O., Oduola, A. M. J., Folarin, O., Keyamo, O., Sowunmi, A., & Happi, C. T. (2010). Rapid Detection of Lactate Dehydrogenase and Genotyping of Plasmodium falciparum in Saliva of Children with Acute Uncomplicated Malaria. Am J Trop Med and Hyg, 83(3), 496–501.

10. Fung, A. O., Damoiseaux, R., Grundeen, S., Panes, J. L., Horton, D. H., Judy, J. W., & Moore, T. B. (2012). Quantitative detection of PfHRP2 in saliva of malaria patients in the Philippines. Malaria J, 11(1), 175.

11. Zia, A.I., Mukhopadhyay, S.C. (2016). Electrochemical Sensing: Carcinogens in Beverages. 1st ed. Springer International Publishing, pp. 21-92.

12. Yuan, X., Song, C., Wang, H. and Zhang, J. (2010). Electrochemical Impedance Spectroscopy in PEM Fuel Cells. 1st ed. Springer, London, pp.95-192.

13. Chang, B., Park, S. (2010). Electrochemical Impedance Spectroscopy. Annual Review of Analytical Chemistry, 3, 207 -229.

14. Lisdat, F., & Schäfer, D. (2008). The use of electrochemical impedance spectroscopy for biosensing. Analytical and Bioanalytical Chemistry, 391(5), 1555–1567.

15. Wang LG, Li YH, Tien HT (1995) Bioelectrochem Bioenerg, 36 (2):145.

16. Berggren C, Bjarnason B, Johansson G (2001) Electroanalysis, 13:173.

17. Radom F. , Jurek P. M., Mazurek M. P.,Otlewski, J., Jelen', F. Dec 2013. Aptamers: Molecules of Great Potential. Biotechnology Advances. Vol 31 Issue 8. P 1260-1274

18. Lakhin A.V., Tarantul V.Z., Gening L.V. Oct-Dec 2013. Aptamers: problems, solutions and Prospects. Acta Naturae. Vol 5 issue 4: p 34-43.

19. Cheung, Y., Kwok, J., Law, A., Watt, R., Kotaka, M. and Tanner, J. (2013). Structural basis for discriminatory recognition of Plasmodium lactate dehydrogenase by a DNA aptamer. Proceedings of the National Academy of Sciences, 110(40), pp.15967-15972.

20. Lee, S., Song, K., Jeon, W., Jo, H., Shim, Y. and Ban, C. (2012). A highly sensitive aptasensor towards Plasmodium lactate dehydrogenase for the diagnosis of malaria. Biosensors and Bioelectronics, 35(1), pp.291-296.

21. Cheung, Y.-W., Dirkzwager, R. M., Wong, W.-C., Cardoso, J., D'Arc Neves Costa, J., & Tanner, J. A. (2018). Aptamer-mediated Plasmodium -specific diagnosis of malaria. Biochimie, 145, 131–136.

22. Chang, B. and Park, S. (2010). Electrochemical Impedance Spectroscopy. Annual Review of Analytical Chemistry, 3(1), pp.207-229.

23. Hoffmann, K. (1974). Applying the Wheatstone bridge circuit. Darmstadt: HBM

24. Ho, W., & Ji, P. (2006). Optimal production planning for PCB assembly. United Kingdom: Springer London.

25. Goodman, P. (2002). Current and future uses of gold in electronics. Gold Bulletin, 35(1), 21–26.

26. Chan, C. M., Tong, K. H., Leung, S. L., Wong, P. S., Yee, K. W., & Bayes, M. W. (2010). Development of novel immersion gold for electroless nickel immersion gold process (ENIG) in PCB applications. In 2010 5th International Microsystems Packaging Assembly and Circuits Technology Conference.

27. Baudrand, D., & Bengston, J. (1995). Electroless plating processes. Metal Finishing, 93(9), 55–57.

28. Chu, M., Nguyen, T. T., Lee, E. K., Morival, J. L., & Khine, M. (2017). Plasma free reversible and irreversible microfluidic bonding. Lab on a Chip, 17(2), 267–273.

29. Fischer, L. M., Tenje, M., Heiskanen, A. R., Masuda, N., Castillo, J., Bentien, A., … Boisen, A. (2009). Gold cleaning methods for electrochemical detection applications. Microelectronic Engineering, 86(4-6), 1282–1285.

30. Heiskanen, A. R., Spégel, C. F., Kostesha, N., Ruzgas, T., & Emnéus, J. (2008). Monitoring of Saccharomyces cerevisiae cell proliferation on Thiol-Modified planar gold Microelectrodes using Impedance spectroscopy. Langmuir, 24(16), 9066–9073.

31. Min, K., Cho, M., Han, S.-Y., Shim, Y.-B., Ku, J., & Ban, C. (2008). A simple and direct electrochemical detection of interferon-γ using its RNA and DNA aptamers. Biosensors and Bioelectronics, 23(12), 1819–1824.

32. Li, Y., Lee, H. J., & Corn, R. M. (2007). Detection of Protein Biomarkers Using RNA Aptamer Microarrays and Enzymatically Amplified Surface Plasmon Resonance Imaging. Analytical Chemistry, 79(3), 1082–1088.